INTERNATIONAL JOURNAL FOR NUMERICAL METHODS IN FLUIDS, VOL. 24, 275–290 (1997)

NUMERICAL STUDY OF EFFECTS OF PULSATILE AMPLITUDE ON UNSTEADY LAMINAR FLOWS IN RIGID PIPE WITH RING-TYPE CONSTRICTIONS

T. S. LEE, T. W. NG AND Z. D. SHI

Mechanical and Production Engineering Department, National University of Singapore, Singapore 119260, Singapore

SUMMARY

The effects of pulsatile amplitude on sinusoidal laminar flows through a rigid pipe with sharp-edged ring-type constrictions have been studied numerically. The parameters considered are: mean Reynolds number (*Re*) of the order of 100; Strouhal number (*St*) in the range 0·0–3·98; Womersley number (*Nw*) in the range 0·0–50·0. The pulsatile amplitude (*A*) varies in the range 0·0–2·0. The flow characteristics were studied through the pulsatile contours of streamline, vorticity, shear stress and isobars. Within a pulsatile cycle the relations between instantaneous flow rate (*Q*) and instantaneous pressure gradient (dp/dz) are observed to be elliptic. The relations between instantaneous flow rate (*Q*) and pressure loss (P_{loss}) are quadratic. Linear relations exist between instantaneous flow rate (*Q*) and maximum velocity, maximum vorticity and maximum shear stress.

KEY WORDS: pulsatile flow; ring-type constrictions; numerical experimentation

1. INTRODUCTION

In recent years, pulsatile flows have attracted much attention owing to their increasing relevance in many engineering and biomedical applications. Unsteady flow through constrictions is of interest to the designer of unsteady flow meters.[1] The relationship between flow rate and pressure loss across various types of constrictions provides a means of estimating the mean flow rate from the measured pressure loss. The principle of unsteady flow has also been frequently applied to heat transfer devices, since heat transfer can be enhanced by the onset of flow instability.[2] In studies of intracardiac flow and stenosis in blood vessels, the pressure loss, maximum flow velocity, shear stress and recirculation region are parameters of extreme interest because of their relationship with the atheroma caused by the large pressure drop across the constriction created through artificial implants, the corpuscle damage due to large shear stress and the thrombus phenomena resulting from the recirculation region.[3–9] In the above studies, parameters of special interest are the pulsatile frequency (*St* or *Nw*) and the pulsatile amplitude (*A*).[1–4] However, most of the above studies are on 'smooth' sinusoidal profiles of bell-shaped constrictions. Few have considered constrictions with sharp edges. Hence an investigation is carried out here to study the effect of amplitude (*A*) variation on unsteady flows through sharp-edged constrictions.

The pulsatile laminar flow in a rigid pipe with a sharp-edged ring-type constriction is used here as a model for studying the application of fluid device implants in intracardiac flow, unsteady flow meters

CCC 0271–2091/97/030275–16

Received November 1995
Revised March 1996

and unsteady flow heat exchangers. Sinusoidal pulsatile flow is the most common type of unsteady flow approximated in most engineering applications. Hence the sinusoidal flow in a rigid pipe with a ring-type constriction is selected as the physical model in the present numerical study.

The objectives of the present work are to investigate the effects of sinusoidal pulsatile amplitude on the developing flow characteristics in a pipe with ring-type constrictions (Figure 1(a)). The effects of pulsatile frequency will also be considered. The investigation will focus on the variation in the pressure gradient along the axial direction, the pressure loss in the flow passing through the constriction, the maximum flow velocity, the maximum vorticity, the maximum shear stress, the recirculation length and the centreline velocity profiles in the developing flow. The results for the ring-type constrictions presented here are limited to $d/D = 0{\cdot}5$ in opening ratio and $h/D = 0{\cdot}1$ in thickness ratio. The mean flow Reynolds number is of the order of 100. The flow Strouhal numbers (St) considered are in the range 0·0–3·98, with the corresponding Womersley numbers (Nw) in the range 0·0–50·0. The pulsatile amplitude (A) varies from 0·0 to 2·0.

2. GROWING EQUATIONS AND NUMERICAL PROCEDURES

The governing equations for axisymmetric unsteady incompressible laminar flow through the constriction shown in Figure 1(a) are given by: continuity equation,

$$\frac{\partial}{\partial z}(ru) + \frac{\partial}{\partial r}(rv) = 0; \tag{1}$$

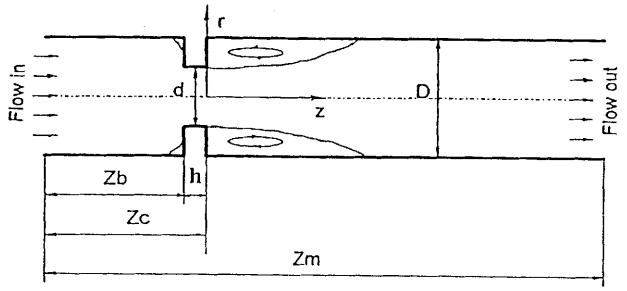

(a) Geometrical configuration

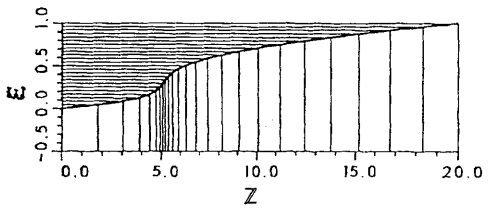

(b) Grid distribution along axial direction

Figure 1. Flow in rigid pipe with sharp edged ring-type constriction

z-direction momentum equation,

$$St\frac{\partial u}{\partial t}+\frac{\partial}{\partial z}(u^2)+\frac{1}{r}\frac{\partial}{\partial r}(ruv)=-\frac{\partial p}{\partial z}+\frac{\partial}{\partial z}\left(\frac{2}{Re}\frac{\partial u}{\partial z}\right)+\frac{1}{r}\frac{\partial}{\partial r}\left[\frac{r}{Re}\left(\frac{\partial u}{\partial r}+\frac{\partial v}{\partial z}\right)\right]; \tag{2}$$

r-direction momentum equation;

$$St\frac{\partial v}{\partial t}+\frac{\partial}{\partial z}(uv)+\frac{1}{r}\frac{\partial}{\partial r}(rv^2)=-\frac{\partial p}{\partial r}+\frac{\partial}{\partial z}\left[\frac{r}{Re}\left(\frac{\partial v}{\partial z}+\frac{\partial u}{\partial r}\right)\right]+\frac{1}{r}\frac{\partial}{\partial r}\left(\frac{2r}{Re}\frac{\partial u}{\partial r}\right)-\frac{1}{Re}\frac{2v}{r^2}. \tag{3}$$

In the solution domain shown in Figure 1(a) the upstream inlet velocity conditions are described by

$$u(r,t)=2\bar{u}(t)[1-(2r/D)^2], \qquad v(r,t)=0{\cdot}0. \tag{4}$$

The bulk inlet velocity $\bar{u}(t)$ is specified as

$$\bar{u}(t)=1+A\sin(2\pi t/T), \tag{5}$$

where A is the pulsatile amplitude. Equation (5) is plotted in Figure 2 for different A-values.

At each time step along the solid wall the no-slip velocity condition is specified by $u=0$ and $v=0$. Along the central line, axisymmetric conditions are applied to all variables, with $\partial u/\partial r=0$, $v=0$ and $\partial p/\partial r=0$. At the downstream exit section the dimensionless pressure is fixed at zero and the flow is considered to be fully developed, so $p=0{\cdot}0$, $\partial u/\partial z=0$ and $\partial v/\partial z=0$.

In a general curvature co-ordinate system (ξ,η), equations (1)–(3) can be expressed as

$$\frac{\partial G}{\partial t}+\frac{\partial}{\partial \xi}(E-M)+\frac{\partial}{\partial \eta}(F-N)-S=0, \tag{6}$$

where

$$\xi=\xi(z,r), \qquad \eta=\eta(z,r). \tag{7}$$

The variables G, E, M, F, N and S in (6) are functions of the physical variables (u, v, p) and the geometrical variables (z, r). They are expressed in detail by Jones and Bajura[1] and Marcelo *et al.*[10] and will not be repeated here.

The curvilinear velocity components U and V in (6) are related to the Cartesian velocity components u and v in (1)–(3) by

$$U=u\xi_z+v\xi_r, \qquad V=u\eta_z+v\eta_r. \tag{8}$$

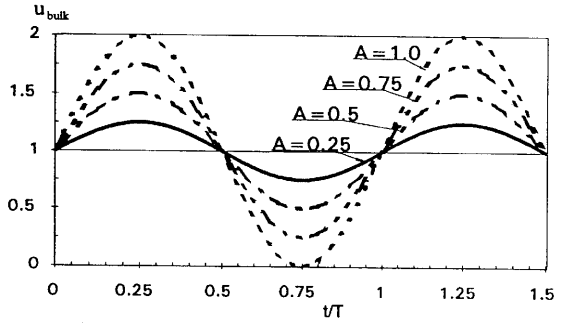

Figure 2. Sinusoidal flow with different amplitudes

The time-dependent term in (4) can be expressed as[3,4]

$$G = \frac{1}{2\pi}\frac{Nw^2}{Re} Jr(0, u, v)^{\mathrm{T}} \tag{9}$$

and the Womersley number Nw is then considered as a characteristic non-dimensional parameter of unsteady flow. The relation between the Strouhal number St and the Womersley number is $Nw = \sqrt{(2\pi Re\, St)}$.

Equation (6) is then solved by an iterative process. All the physical variables (u, v, p) are updated through

$$\phi^{n+1} = \phi^n + \delta\phi, \tag{10}$$

where n and $n+1$ are the previous and current iteration numbers respectively and ϕ represents any of the physical variables. Substituting equation (10) into (6), the governing equations can be expressed in incremental form as

$$\frac{\partial \delta G}{\delta t} + \frac{\partial}{\partial \xi}(\delta E - \delta M) + \frac{\partial}{\partial \eta}(\delta F - \delta N) - \delta S = -R. \tag{11a}$$

The residual vector R is calculated using the value of the variable at level n as

$$R = \frac{\partial G^n}{\partial t} + \frac{\partial}{\partial \xi} + \frac{\partial}{\partial \xi}(E - M)^n + \frac{\partial}{\partial \eta}(F - N)^n - S^n. \tag{11b}$$

Equations (11) are solved by the SIMPLE algorithm[11] on a non-staggered grid. The grid point distribution within the solution domain is shown in Figure 1(b). A stretching function is used along the axial direction,

$$\frac{\mathrm{d}z}{\mathrm{d}\xi} = a_{\mathrm{m}}[\alpha + \beta(\xi - \xi^1)^2\gamma^{\xi}], \tag{12a}$$

with the boundary conditions given by

$$z|_{\xi=0} = 0, \qquad z|_{\xi=1} = z_{\mathrm{m}}, \tag{12b}$$

where z_m is the maximum length of the solution domain in the axial direction and α and γ are two grid control parameters. At point $\xi = \xi_1$ the grid size is $\Delta z = z_{\mathrm{m}}\alpha\Delta\xi$, which can be controlled through the value of α. If $\alpha < 1{\cdot}0$, the grid will become more clustered at point $\xi = \xi_1$. The grid distribution in the z-direction can be further refined through the parameter γ.

With the grid distribution as defined by (12), all terms containing the incremental variables $(\delta E, \delta M, \delta F, \delta N, \delta S)$ are discretized by three-point difference schemes. Hybrid difference schemes are used for convective terms, second-order central schemes for diffusive terms, first-order forward schemes for pressure terms and first-order backward schemes of the continuity equation. The residual vector is calculated by second-order difference schemes: second-order upwind schemes for convective terms, second-order central schemes for diffusive terms, second-order forward schemes for pressure terms and second-order backward schemes for the continuity equation. At convergence the residual vector R is equal to zero and the convergent results have second-order accuracy. For points adjacent to the wall the corresponding second-order difference schemes are also used to ensure consistency of the scheme accuracy.

For the time-dependent terms a modified Crank–Nicolson scheme is used to discretize the governing equations,

$$\frac{\delta G^{n+1} - \delta G^n}{\Delta t} + \theta X^{n+1} + (1 - \theta)X_n = -R, \tag{13}$$

where

$$X = \frac{\partial}{\partial \xi}(\delta E - \delta M) + \frac{\partial}{\partial \eta}(\delta F - \delta N) - \delta S$$

and θ is a scheme control parameter ranging from 0·0 to 1·0; $\theta = 0{\cdot}0$ is for the time-explicit scheme, $\theta = 1{\cdot}0$ is for the time implicit scheme and $\theta = 0{\cdot}5$ is for the standard Crank–Nicolson scheme. The optimum θ-value in the present numerical computation is determined from numerical experiments to obtain stable and convergent results. In the present work, $\theta = 0{\cdot}6$ is chosen.

Second-order discretizations of the pressure gradient terms and the continuity equation are adjusted according to the instantaneous main flow direction. This numerical scheme was found to be the most accurate and numerically stable for the pulsatile flow problems studied here.

The numerical procedure for the pulsatile flow computation adopted in this study can be briefly outlined as follows.

1. The steady flow is computed and taken as initial condition for the unsteady flow computation. At the advancement of each time step the initial velocity and pressure fields are given by the converged values of the previous time step and the boundary values of each variable are specified.
2. The momentum equations are solved by sweeping in the positive and negative *r*-direction with an underrelaxation procedure. The underrelaxation factor is 0·35. The residual of each equation is computed. Iteration is continued until the residuals of all the equations reduce to 0·1% of their values at the first iteration.
3. The residual of the continuity equation is computed and used as the source term of the pressure correction equation, which is then solved by ADI sweeps. The sweep is repeated until the residual of the pressure correction equation reduces to 0·1% of its value at the first iteration.
4. The flow flux at each section in the *z*-direction is computed. The maximum equation residual and maximum flux difference from that at the inlet section are obtained. The programme will return to step 2 when the maximum residual or maximum flux difference is greater than 0·1% of the initial value.
5. At convergence the streamline, vorticity and shear stress fields are computed from the velocity field. Information about the pressure is obtained from the pressure field.

3. RESULTS AND DISCUSSION

For the computation of the flow field in a pipe with a ring-type constriction, non-uniform grids were used in the axial *z*-direction, with more grid points being distributed nearer the constriction as shown in Figure 1(b). For the radial direction and the time domain, computational grids were evenly distributed. Grids with 15, 21 and 31 points in the *r*-direction and 81, 101, 121 and 141 points in the *z*-direction were tested. Grids with 31, 41 and 51 points per pulsatile period (T) in the time domain were tested for the first three time periods to check on the grid point independency of the numerical results obtained. Further computations are then based on a grid point arrangement of 21, 121 and 41 in the *r*-, *z*- and *t*-direction respectively. Computations were carried out for more than one periodic time cycle for every pulsatile unsteady flow condition considered.

The validity of the numerical procedure and grid size was first checked against available data for steady laminar flow in a sudden expansion pipe. Test results are compared with similar data from Reference 12 and 13 for the recirculation length and the wall shear stress in Figure 3. The results indicate that the present numerical procedure and grid size produce accurate results when compared

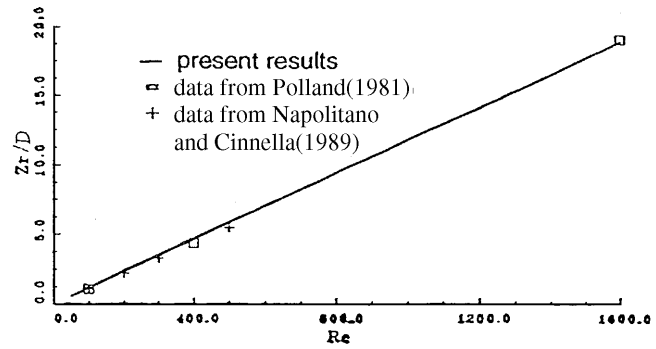

(a) the recirculation lengths

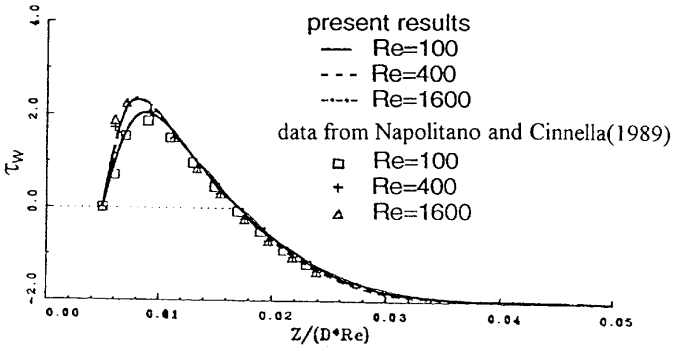

(b) the wall shear stress distribution

Figure 3. Comparison of results on steady flow in pipe with sudden expansion

with known steady laminar flow data. It is thus assumed that a similar procedure and grid size should also produce accurate results for the unsteady laminar flow cases to be considered here.

Sinusoidal flows with dimensionless amplitude A varying from 0·0 to 2·0 were computed for different Strouhal numbers and Womersley numbers. Figure 4 displays typical characteristics of the development of a sinusoidal flow field ($St = 0{\cdot}04$, $A = 1{\cdot}0$) with respect to time t/T in a pipe with a ring-type constriction. It shows the developments of the streamline field, the vorticity field and the distributions of shear stress and isobars. It should be noted here that as t/T advances from 0·0 to 1/4, the forward flow is accelerated to the peak flow velocity. The recirculation length z_r/D increases from its steady flow value to a maximum value. As t/T further advances from 1/4 to 3/4, the forward flow is decelerated back towards its minimum value and z_r/D decreases to its minimum value correspondingly. During the period of t/T from 3/4 to 1·0, when the flow velocity is accelerated back to its maximum value again, z_r/D increases from its minimum value back to its maximum value. When t/T further advances from 1·0 to 6/4, the second cycle starts and the flow follows a repeated pattern. The changes in recirculation length are presented in Figure 5 for different values of amplitude ($A = 0{\cdot}25$–$1{\cdot}0$). The results show that the recirculation region in the unsteady flow domain is not stationary. For the duration where the instantaneous bulk velocity of the flow field is very small, the

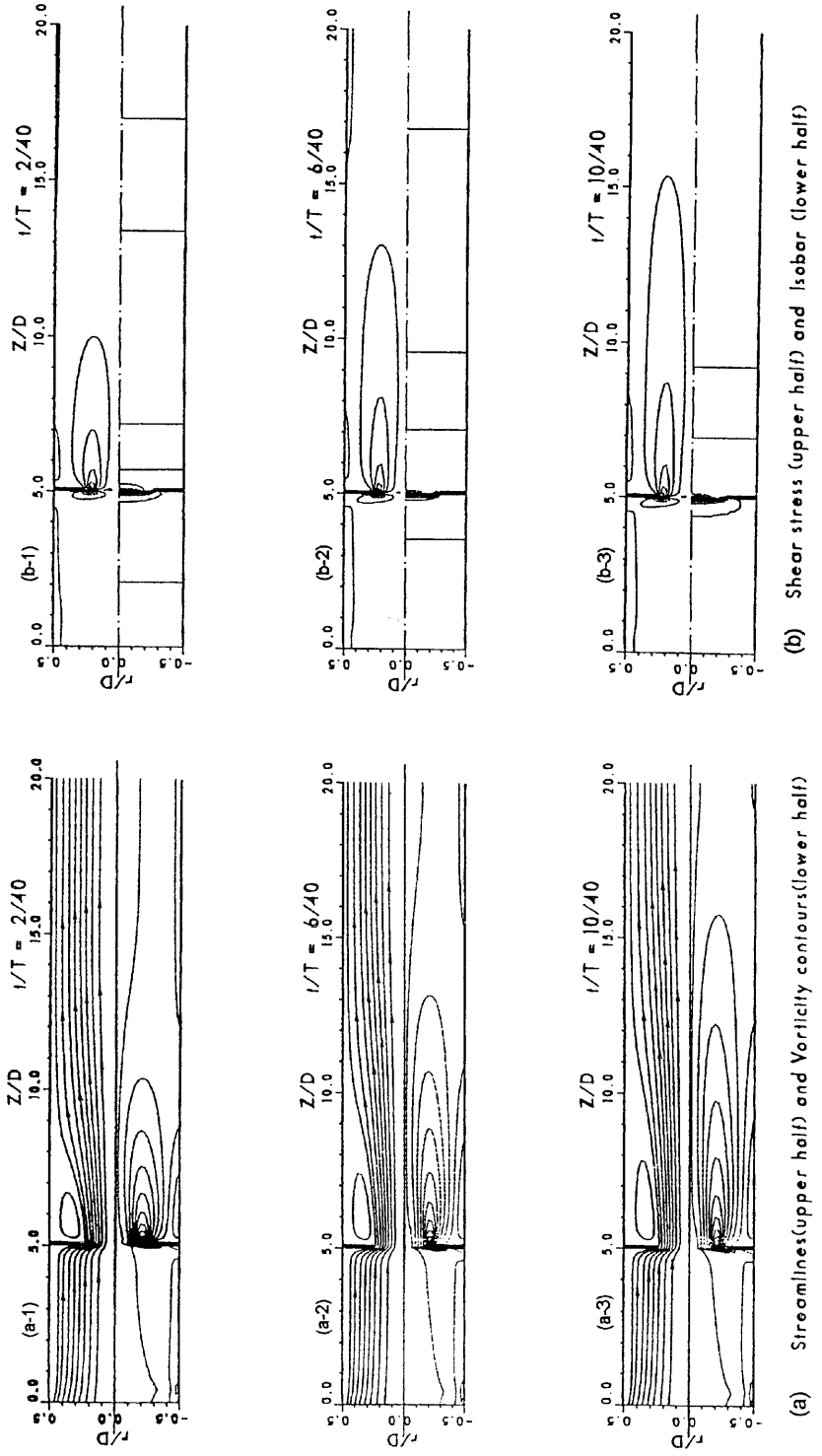

Figure 4a. Sinusoidal flow development in pipe with ring-type constriction ($d/D = 0{\cdot}5$, $h/D = 0{\cdot}1$, $Re = 100$, $St = 0{\cdot}04$, $Nw = 5{\cdot}01$, $A = 1{\cdot}0$)

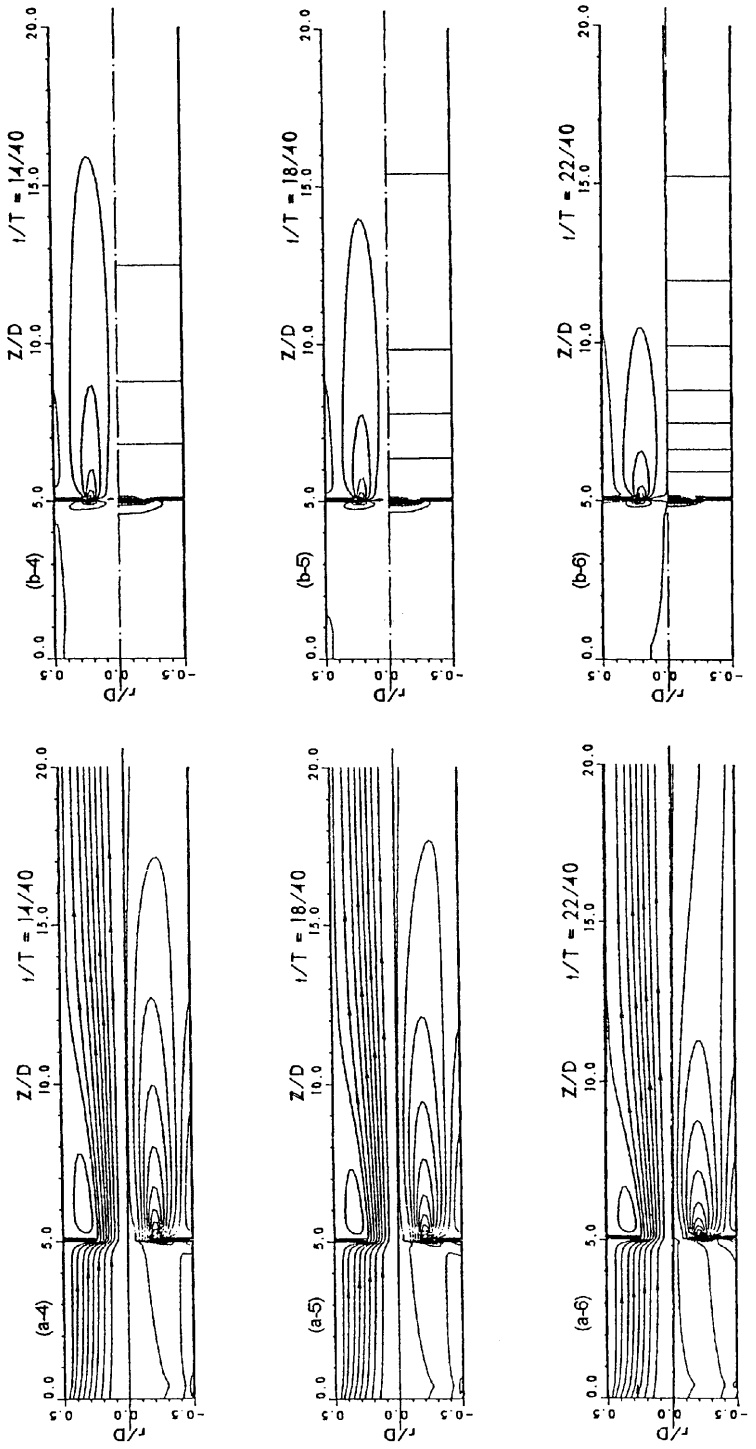

Figure 4b. Sinusoidal flow development in pipe with ring-type constriction ($d/D = 0{\cdot}5, h/D = 0{\cdot}1, Re = 100, St = 0{\cdot}04, Nw = 5{\cdot}01, A = 1{\cdot}0$)

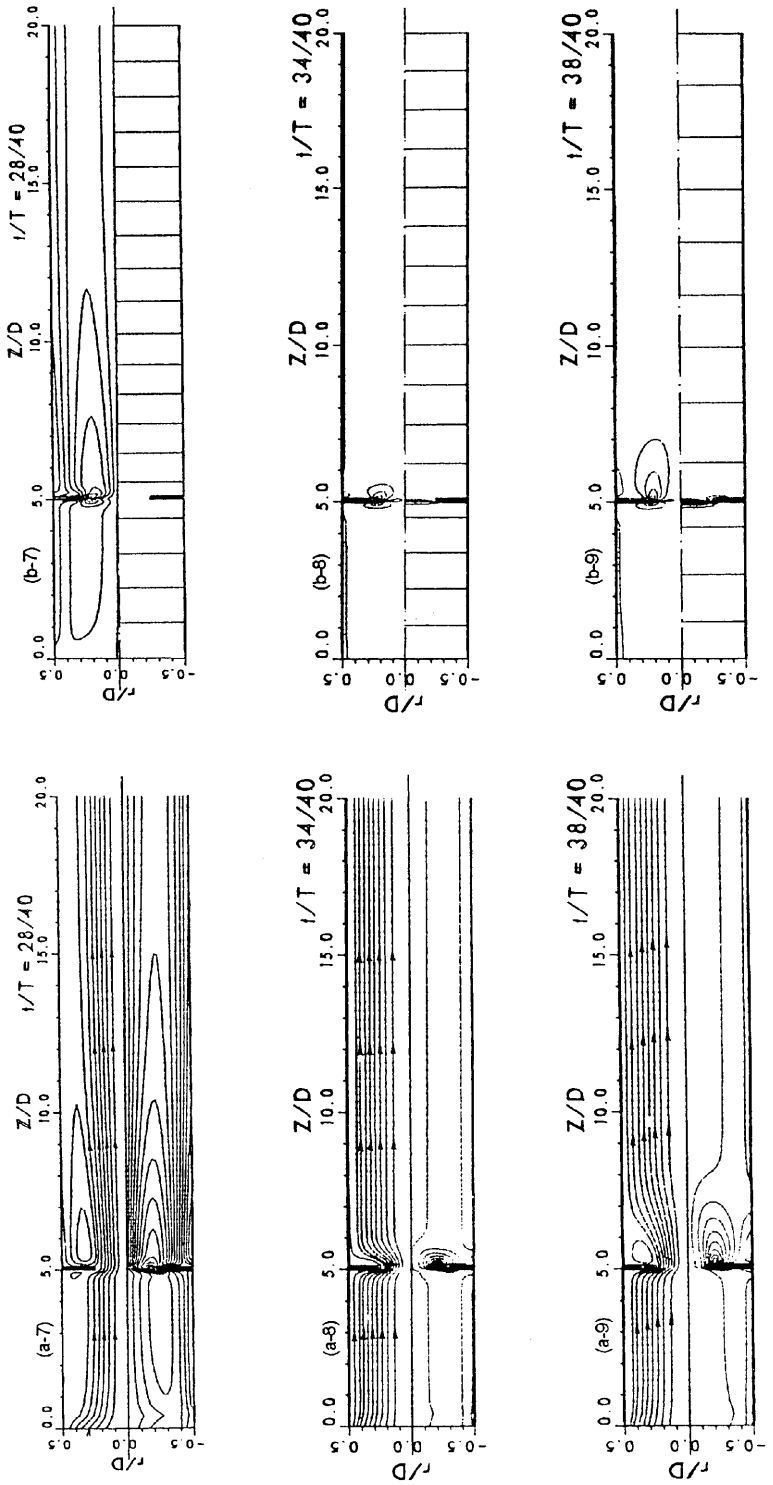

Figure 4c. Sinusoidal flow development in pipe with ring-type constriction ($d/D = 0{\cdot}5$, $h/D = 0{\cdot}1$, $Re = 100$, $St = 0{\cdot}04$, $Nw = 5{\cdot}01$, $A = 1{\cdot}0$)

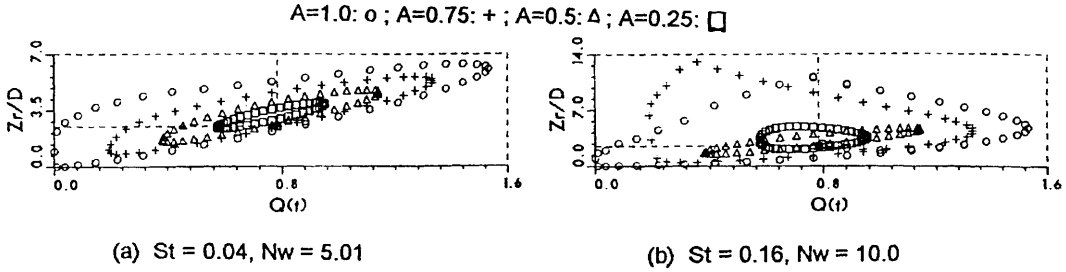

Figure 5. Relation between flow rate and recirculation length

recirculation region in the flow domain is negligible. For the sinusoidal flow investigated, flow acceleration and deceleration are of the same magnitude at the same instantaneous flow rate Q. However, as shown in Figure 4 through the development of the streamlines and in Figure 5 through the development of the recirculation length, it is noted that during the deceleration phases the flow field results in a larger recirculation region.

The centreline velocity is also an important flow characteristic in the study of unsteady flow field development. As seen in Figure 6 for $A = 0{\cdot}5$ and $1{\cdot}0$, the centerline velocity distribution along the axial direction shows a similar periodic change to the unsteady flow field. The time levels (t) are given on each figure. The time step used is $\Delta t = 1/40$. From the study of other figures in Figure 6, for $A = 1{\cdot}0$ the flow is nearly stationary at time levels 30 and 32. With the bulk velocity approaching zero, the recirculation length also approaches zero.

Typical relations between instantaneous flow rate Q and instantaneous pressure gradient $\mathrm{d}p/\mathrm{d}z$ along the axial direction in the fully developed flow region at $z/D = 16$ are shown in Figure 7. The $\mathrm{d}p/\mathrm{d}zQ$ instantaneous values show an elliptic relation.

From the above the time-averaged pressure gradient $\overline{\mathrm{d}p}/\mathrm{d}z$ is obtained from

$$\overline{\mathrm{d}p/\mathrm{d}z} = \int_{0{\cdot}5}^{1{\cdot}5} (\mathrm{d}p/\mathrm{d}z)\mathrm{d}t. \tag{14}$$

Typical trends and results are presented in Figure 8. As the amplitude A increases, the magnitude of $\overline{\mathrm{d}p/\mathrm{d}z}$ decreases and approaches a stationary value. The dimensional time-averaged pressure gradient can be obtained from

$$\overline{\mathrm{d}p/\mathrm{d}z^*} = (\overline{\mathrm{d}p/\mathrm{d}z})(Re\mu)^2/\rho D^3. \tag{15}$$

Relations between instantaneous flow rate Q and pressure loss P_{loss} across the constriction are presented in Figure 9 for different dimensionless amplitudes. The empirical relationship obtained through the numerical experiments can be expressed as

$$P_{\mathrm{loss}} = C_{\mathrm{ploss}} Q|Q| \tag{16}$$

where $C_{\mathrm{ploss}} = 15{\cdot}0$ for $St = 0.04$ and $C_{\mathrm{ploss}} = 14{\cdot}8$ for $St = 0{\cdot}16$.

Variations in time-averaged pressure $\bar{P}_{\mathrm{loss}}$ with respect to pulsatile amplitude are shown in Figure 10. $\bar{P}_{\mathrm{loss}}$ is seen to increase with the pulsatile amplitude. However, the difference between the characteristic trends for Strouhal numbers of $0{\cdot}04$ and $0{\cdot}16$ is negligible.

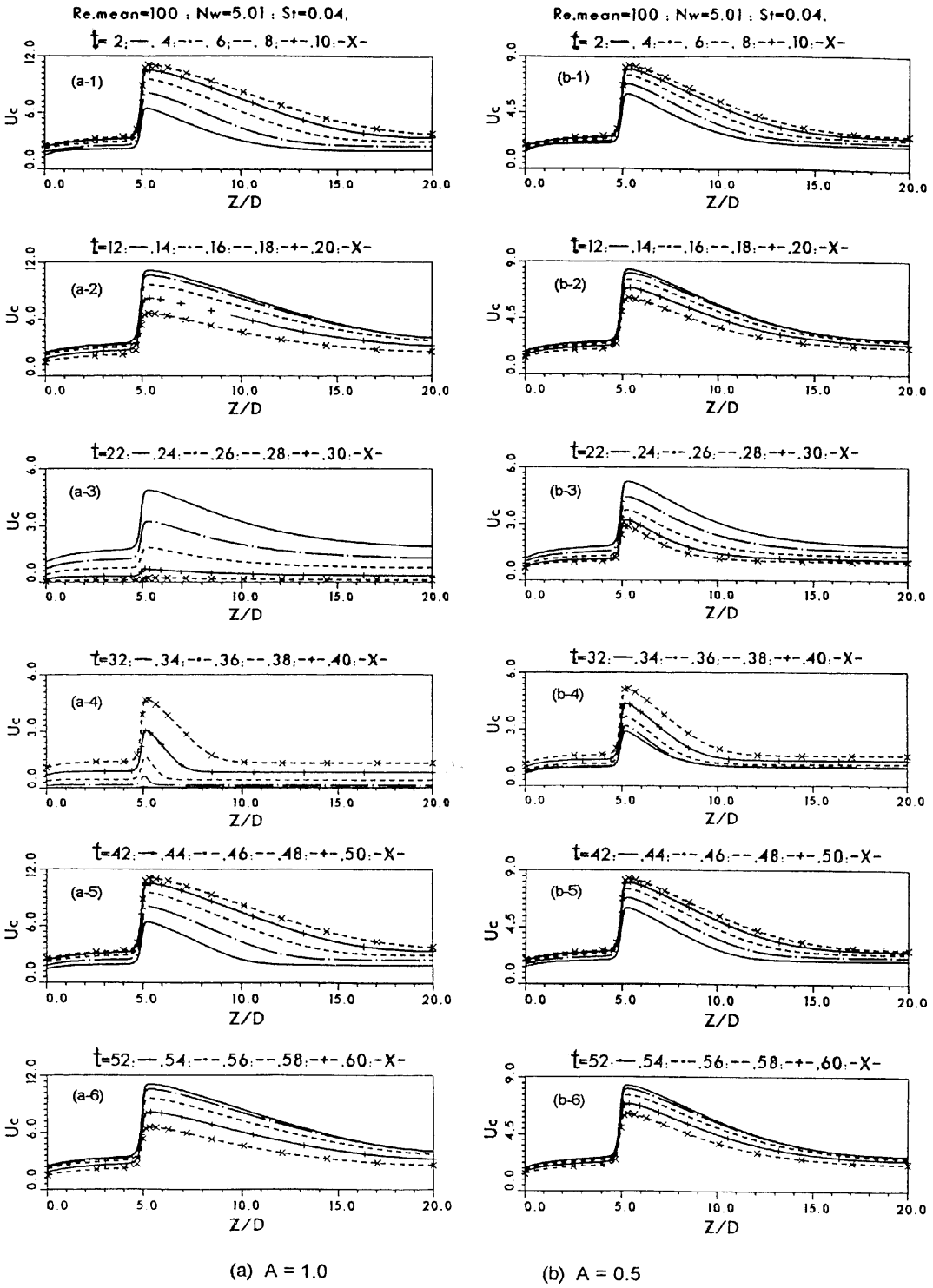

Figure 6. Centreline velocity development of sinusoidal flows

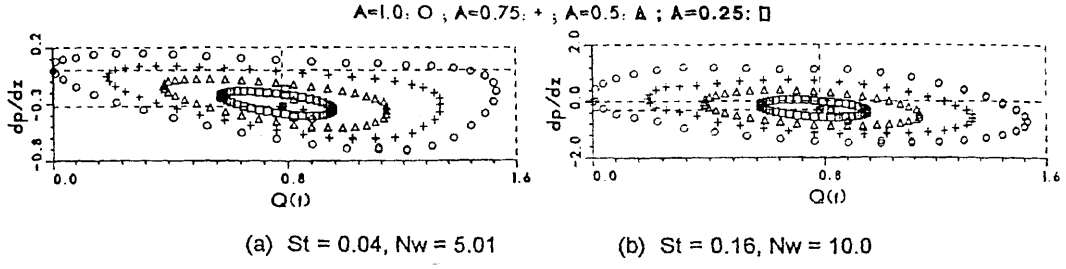

Figure 7. Relation between flow rate and axial pressure gradient

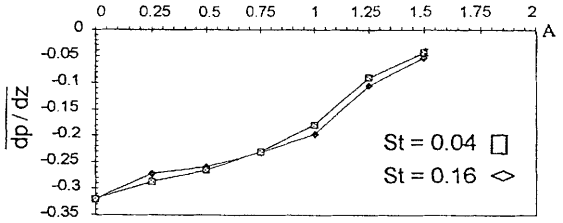

Figure 8. Effect of pulsatile amplitude on time-averaged axial pressure gradient

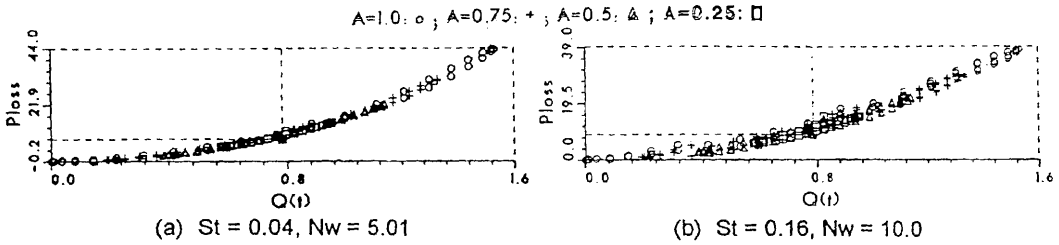

Figure 9. Relation between flow rate and pressure loss

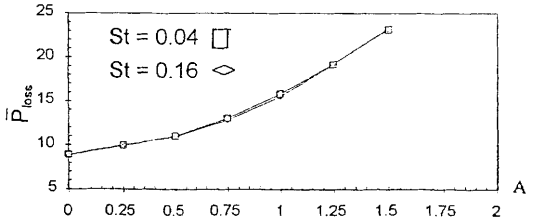

Figure 10. Effect of pulsatile amplitude on time-averaged pressure loss

Other parametric relations of laminar sinusoidal flow fields that can be obtained through the present study include linear relations between flow rate and non-dimensional maximum values of overall flow velocity, vorticity and shear stress. These are expressed as

$$u_{\max} = 6{\cdot}88Q(t), \qquad \Omega_{\max} = 162{\cdot}26Q(t), \qquad \tau_{\max} = 1{\cdot}05Q(t) \tag{17}$$

and illustrated in Figures 11–13 for $St = 0{\cdot}04$ and $0{\cdot}16$. As expected, the maximum flow velocity is always located on the centerline of the pipe (Figure 11). The corresponding maximum wall vorticity and shear stress are presented in Figures 14 and 15. For $St = 0{\cdot}04$, linear relations between $Q(t)$ and both $\Omega_{w,\max}$ and $\tau_{w,\max}$ are given by

$$\Omega_{w,\max} = 16{\cdot}09Q(t), \qquad \tau_{w,\max} = 0{\cdot}189Q(t). \tag{18}$$

The maximum wall vorticity and shear stress are of the order of $1/10$ and $1/5$ of their overall maximum field values respectively (Figures 12–15). In related biofluid dynamic investigations, such as intracardiac flow and valvular regurgitant flow studies, information on the velocity field is obtained from the Doppler echo cardiography technique.[14]

4. CONCLUSIONS

The effects of pulsatile amplitude on the flow fields through a sharp-edged ring-type constriction were investigated for A in the range 0·0–2·0, Nw from 0·0 to 50·0 and St from 0·0 to 3·98. Numerical experiments show that flow deceleration in the pulsatile cycles tends to enlarge the recirculation region and this effect becomes more significant with an increase in pulsatile amplitude (or corresponding increase in Womersley and Strouhal numbers). The corresponding flow acceleration in the pulsatile cycles tends to increase the pressure drop in the pipe flow. Other more specific flow

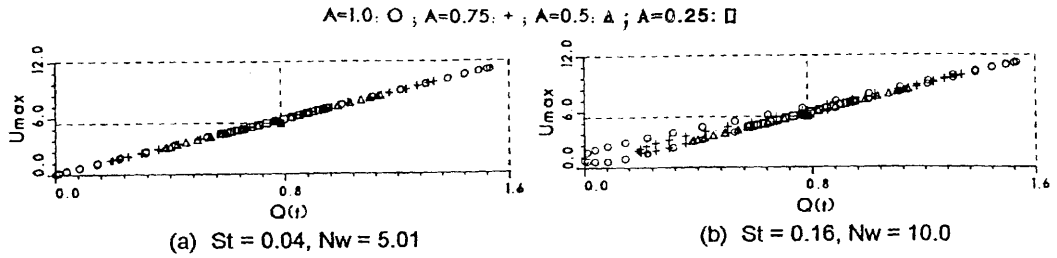

Figure 11. Relation between flow rate and maximum velocity

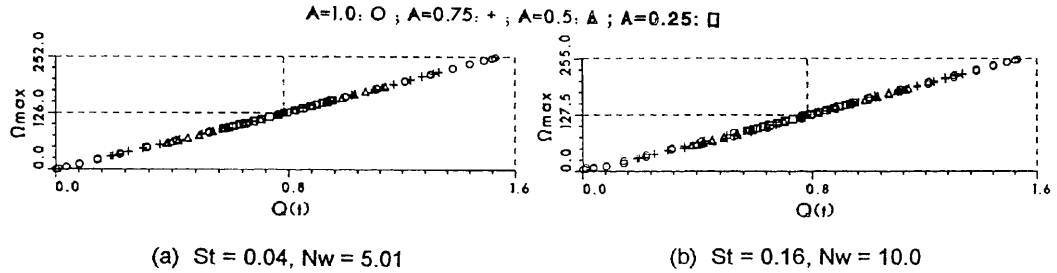

Figure 12. Relation between flow rate and maximum vorticity

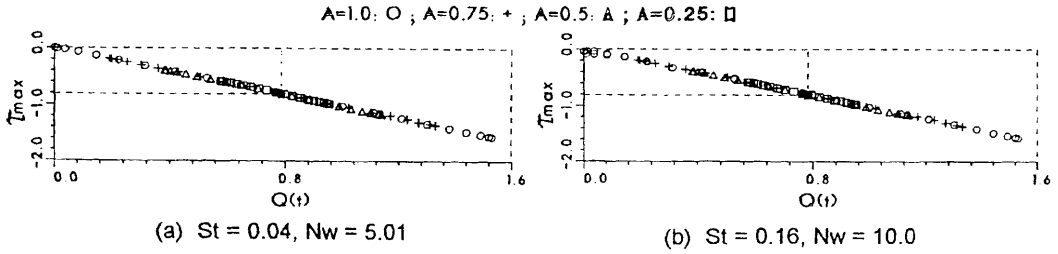

Figure 13. Relation between flow rate and maximum shear stress

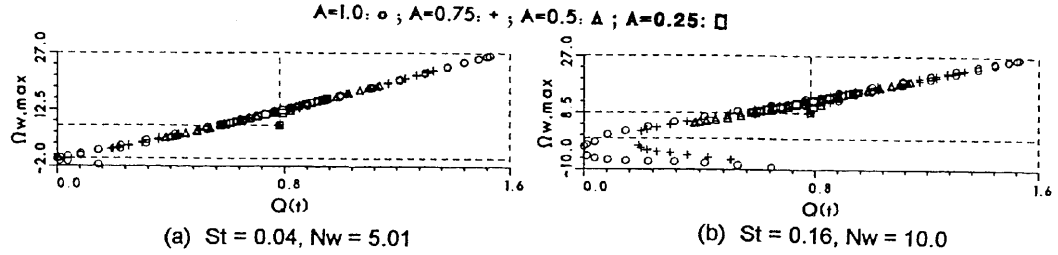

Figure 14. Relation between flow rate and maximum wall vorticity

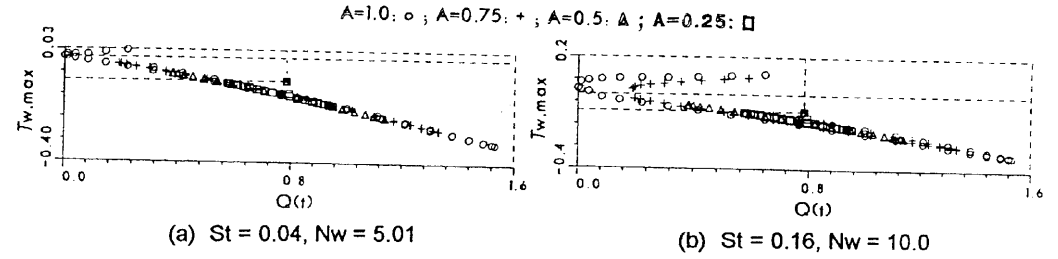

Figure 15. Relation between flow rate and maximum wall shear stress

characteristics are also observed. The relationship between instantaneous flow rate and pressure loss across the constriction is quadratic. However, the relationship between instantaneous flow rate and pressure gradient is elliptic. The time-averaged pressure gradient along the axial direction tends towards a stationary value when the pulsatile amplitude is increased from 0·0 to 2·0. Other linear relations exist between flow rate and maximum velocity, maximum vorticity and maximum shear stress within the pulsatile flow field.

APPENDIX: NOMENCLATURE

a	pulsatile amplitude
A	dimensionless pulsatile amplitude, a/D
d	orifice diameter
D	pipe diameter (characteristic length)
h	constriction thickness
Nw	Womersley number, $D\sqrt{(\omega/\nu)}$

p	pressure
$\mathrm{d}p/\mathrm{d}z$	pressure gradient in axial direction
$\overline{\mathrm{d}p/\mathrm{d}z}$	time-averaged pressure gradient, $(1/T)\int_t^{t+T}(\mathrm{d}p/\mathrm{d}z)\mathrm{d}t$
P_{loss}	pressure loss across constriction, pressure different between upstream and downstream flow
$\bar{P}_{\mathrm{loss}}$	time-averaged pressure loss, $(1/T)\int_t^{t+T} P_{\mathrm{loss}}\mathrm{d}t$
Q	flow rate, $Q(t) = (\pi/4)D^{2-}u(t)$
$Q_{\max}$	maximum flow rate, 1·0
r	radial co-ordinate, radial distance
Re	Reynolds number, $\bar{u}_{\mathrm{peak}}D/\nu$
St	Strouhal number, $D/\bar{u}_{\mathrm{peak}}T$ or $(1/2\pi)Nw^2/Re$
t	time co-ordinate, time-step
T	time period of physiological flow
T_{s}	time period of sinusoidal flow
u	axial velocity component
$\bar{u}(t)$	instantaneous bulk velocity in pipe
$\bar{u}_{\mathrm{peak}}$	peak $\bar{u}(t)$-value (characteristics velocity)
v	radial velocity component
z	axial co-ordinate, axial distance
z_{r}	recirculation length

Greek letters

α_{p}	underrelaxation factor in updating pressure
ξ,η	co-ordinate variables in general curvature co-ordiante system
ν	fluid molecular kinetic viscosity
ρ	density of fluid
τ	shear stress, $(1/Re)(\partial u/\partial r) + (\partial v/\partial z)$
Ω	vorticity, $\partial u/\partial r - \partial v/\partial z$

REFERENCES

1. E. H. Jones Jr. and R. A. Bajura, 'A numerical analysis of pulsating laminar flow through a pipe orifice', *ASME J. Fluids Eng.*, **113**, 199–205 (1991).
2. H. Suzuki, Y. Inoue, T. Nishimura, K. Fukutani and K. Suzuki, 'Unsteady flow in a channel obstructed by a square rod (crisscross motion of vortes)', *Int. J. Heat Fluid Flow*, **14**, 2–9 (1993).
3. L. M. Strivastava, 'Flow of couple stress fluid through stenotic blood vessels', *J. Biomech.*, **18**, 479–485 (1985).
4. N. Masahide and S. Tadashi, 'Numerical study on the unsteady flow of non-Newtonian fluid', *ASTEM J. Biomech. Eng.*, **112**, 100–103 (1990).
5. H. Huang, V. J. Modi, B. R. Seymour and R. Ralida, 'Fluid dynamics of stenosed arteries: a numerical study', *Proc. 6th Int. Conf. on Biomedical Engineering*, 1990, pp. 435–540.
6. Z. Lou and W. J. Yang, 'A computer simulation of the non-Newtonian blood flow at the aortic bifurcation', *J. Biomech.*, **26**, 37–49 (1993).
7. T. S. Lee, 'Numerical studies of fluid flow through tubes with double constrictions.' *Int. j. numer. methods fluids*, **11**, 1113–1126 (1990).
8. T. S. Lee, 'Steady laminar fluid flow through variable constrictions in vascular tubes', *J. Fluids Eng.*, **116**, 66–71 (1994).
9. T. S. Lee and H. T. Low, 'Separation and reattachment of fluid flow through series vascular constriction', *J. Finite Elem. Anal. Des.*, **18**, 365–377 (1994).
10. R. Marcelo, A. Mahamad and C. Ricardo, 'Computation of incompressible turbulent flows by an opposed-differencing scheme', *Numer. Heat Transfer*, **12**, 307–320 (1987).
11. S. V. Patankar, *Numerical Heat Transfer and Fluid Flow*, Hemisphere, Washington, DC 1980.
12. A. Polland, 'A contribution on the effects of inlet conditions when modelling stenosis using sudden expansions', *J. Biomech.*, **14**, 349–355 (1981).

13. M. Napolitano and P. Cinnella, 'A numerical study of planar and axially-symmetric suddent expansion flows', *Comput. Fluids*, **17**, 185–193 (1989).
14. A. S. Pearlman and C. M. Otto, 'Quantification of valvular regurtitant: a review of cardiovascular ultrasound', *Echocardiography*, **4**, 271–287 (1987).
15. D. A. McDonald, 'The relation of unsteady pressure to flow in arteries', *J. Physiol.*, **127**, 533–552 (1955).
16. W. Y. Soh and J. W. Goodrich, 'Unsteady solutin of incompressible Navier–Stokes equations', *J. Comput. Phys.*, **79**, 113–134 (1988).
17. D. A. Steinman, Bach Vinh, C. R. Ethier, M. Ojha, R. S. C. Cobbold and K. W. Johnson, 'A numerical simulation of flow in a two-dimensiona end-to-side anastomosis model', *ASME J. Biomed. Eng.*, **115**, 112–118 (1993).
18. H. Suzuki, Y. Inoue, T. Nichimura, K. Fukutani and K. Suzuki, 'Unsteady flow in a channel obstructed by a square rod (crisscross motion of vortes)', *Int. J. Heat Fluid Flow*, **14**, 2–9 (1993).